remote sensing

MDPI

Article

Obtaining 3D High-Resolution Underwater Acoustic Images by Synthesizing Virtual Aperture on the 2D Transducer Array of Multibeam Echo Sounder

Bo Wei [1,2,3], Haisen Li [1,2,3], Tian Zhou [1,2,3,*] and Siyu Xing [1,2,3]

[1] Acoustic Science and Technology Laboratory, Harbin Engineering University, Harbin 150001, China; weibo@hrbeu.edu.cn (B.W.); hsli@hrbeu.edu.cn (H.L.); xingsiyu@hrbeu.edu.cn (S.X.)
[2] Key Laboratory of Marine Information Acquisition and Security (Harbin Engineering University), Ministry of Industry and Information Technology, Harbin 150001, China
[3] College of Underwater Acoustic Engineering, Harbin Engineering University, Harbin 150001, China
* Correspondence: zhoutian@hrbeu.edu.cn; Tel.: +86-0451-82589147

Received: 1 September 2019; Accepted: 7 November 2019; Published: 8 November 2019

Abstract: In recent decades, imaging sonar has been the most widely employed remote sensing instruments in the field of underwater detection. The multibeam echo sounder (MBES) plays an important role in obtaining high-accuracy seabed topography. However, the resolution of the MBES substantially decreases with the increasing distance. Synthetic aperture sonar (SAS) achieves constant resolution on the along-track, improving the fineness of the image. However, conventional side-scan SAS usually only achieves 2D images, and gaps always exist. In this modeling and experimental research paper, we propose a novel underwater acoustic imaging scheme to improve the imaging performance of MBES, based on the complementarity of MBES and SAS systems. We design a 2D transducer array to increase the detection efficiency and obtain spatial gain. Moreover, the processing scheme is analyzed to design the working parameters in actual engineering applications. We exploit a target echo simulation approach to establish the research basics of the imaging algorithms, which also reflects the shapes and shadows of targets to match actual situations as realistically as possible. The proposed imaging algorithm synthesizes a virtual aperture receiving array on the along-track and reserves the multi-element manifold on the across-track. This helps to improve the imaging quality of the MBES and achieves high-resolution 3D detection with no gaps. Simulation and tank experimental results demonstrate that the proposed scheme can significantly improve the detection ability of the MBES, especially for small 3D target detection, thus making it suitable for 3D high-resolution underwater detection applications.

Keywords: multibeam echo sounder; underwater acoustic imaging; 2D transducer array; 3D high-resolution detection

1. Introduction

Imaging sonar systems are major remote sensing instruments that require a high resolution to guarantee detection accuracy that has many technology branches [1]. The multibeam echo sounder (MBES) has been widely used in recent decades as an effective underwater acoustic detection instrument. The MBES achieves full-scan 3D detection in the whole detecting area through carrier movement and imaging mosaic methods. Water column and snippet side scan imaging are also practical technology of MBES to detect fish schools or bottom targets in detail [2–4]. However, the resolution of the MBES on the along-track and across-track both decreases substantially with an increasing beam width and distance. Synthetic aperture sonar (SAS) is used as a kind of imaging sonar that can provide a constant high resolution on the along-track, independent of the echo frequency and distance [5,6]. SAS can

provide a detailed backscattered acoustic image that is widely employed, e.g., for cables and unexploded ordnance detection. In most recent research, SAS systems are usually based on the echo model of side-scan sonar (SSS), which also introduces disadvantages such as the gap problem and have to employ an additional MBES as the gap filler [7,8]. Furthermore, conventional SAS usually achieve 2D images that just indicate the azimuth and range direction. Accurate depth information of the targets cannot be obtained directly from SAS images [9,10]. Although some interferometric synthetic aperture sonar (InSAS) or multi-receiver SAS can estimate depth information through phase differences between the multiple elements on the along-track, the depth accuracy of InSAS is much lower than that of MBES, which is usually employed as an assistant reference. Multi-receiver SASs usually employ only several elements on the along-track, which is much less than the dozens or even hundreds of receivers placed by the MBES [11]. The scale of the transducer array limits the depth estimation accuracy of InSAS.

Multibeam synthetic aperture sonar (MBSAS) is proposed as a novel imaging sonar technology that effectively overcomes the disadvantages of MBES and SAS but has been rarely researched. MBSAS achieves a 3D full-scan detecting with no gaps problem and more accurate height detection, compared with SAS. Higher resolution can also be obtained through the synthesizing virtual aperture on the along-track, compared with MBES. MBSAS could be achieved through the MBES scheme or other 2D transducer arrays and is suitable to be employed in the field of detailed underwater surveys. Some basic research of MBSAS has been carried out, such as the basic echo model of a single-line MBSAS system [12]. The feasibility of single-line MBSAS is verified preliminarily through a tank experiment [13]. Motion error and its influence on the imaging and estimation algorithm of the 2D transducer array have also been proposed [14]. However, the complete theoretical system of MBSAS has not been fully discussed. The target simulation, processing scheme, and working conditions of MBSAS are also research domains where the system could be shown to be efficient and valuable. In this paper, we propose a novel underwater acoustic imaging scheme to improve the imaging performance of MBES, based on the complementarity of MBES and SAS systems. The transducer array and signal processing scheme are analyzed to design the working parameters for engineering applications. For targets with shadow, a simulation approach is introduced to generate MBSAS echoes. We propose an imaging algorithm that integrates the theories of MBES and SAS to provide high-resolution detection in 3D space. A principle prototype of MBSAS is also designed to verify the proposed theory. The performance of the novel instrument is demonstrated through simulations and tank experiments. We also discuss the working conditions and prospect of the novel device.

2. Echo Model and Processing Scheme of MBSAS

2.1. Basic Echo Model of MBSAS

MBSAS combines the technical characteristics of MBES and SAS so that the array manifold is specially designed. The 2D MBSAS system employs a uniform linear array (ULA) with a number of receiving elements on the across-track, as in the conventional MBES. There are also several linear receiving arrays located on the along-track that form a planar transducer array. The proposed 2D transducer array model is shown in Figure 1a. The MBSAS system needs a larger beam angle width on the along-track than MBES to illuminate the target more times on the trajectory. Therefore, we designed a transmitter located on the edge of the receiving array, which is different from the behind side as in the conventional MBES. The sampling interval on the along-track is limited by the principle of SAS imaging, which requires the carrier to move slowly to ensure signal synthesis [15]. The element on the along-track is first processed by the synthetic aperture, and then a virtual line receiving array is obtained on the across-track. Beamforming processing is carried out on the virtual array to divide the across-track into beam-space. A planar transducer array can increase the detection efficiency because echoes can also be received by the elements on the along-track.

The sampling interval on the along-track limits the quality of the synthesizing algorithm. A high carrier moving speed will introduce a grating lobe problem, which is also synthesized in the imaging

processing. Thus, the carrier speed is limited in order to guarantee the effectiveness of the imaging algorithm, which reduces the sonar detection efficiency. The multiple elements on the along-track can manage this problem by receiving more echoes at different detected angles in a single synthesized aperture period so that the carrier speed can be increased. A wideband signal can also be managed to solve the grating lobe problem. MBSAS employs linear frequency modulated (LFM) signals to provide a large time-bandwidth product and high distance resolution, which is widely used in SSS and SAS systems [16,17]. The synthetic processing occurs through the motion of the carrier so that a virtual aperture array is generated on the along-track. The 2D transducer array still keeps the multi-element transducer array manifold on the across-track. Finally, as shown in Figure 1a, the 2D transducer array is converted to a virtual ULA which has a large aperture on the along-track and keeps the manifold as MBES on the across-track. The processing scheme is discussed in detail in Section 2.2.

In actual applications, the elements and the bandwidth cannot be increased boundlessly, but are inevitably limited by the transducer array manufacturing process and the cost. We compromised by applying the echo synthesis algorithm in a very narrow space just below the carrier to avoid the grating lobe problem. An image of the whole detected area can also be obtained by moving the carrier. We designed a 2D array structure that has 4 ULAs, and each ULA has 32 receiving elements. Thus, we can research some imaging algorithms based on the subarray structure with the beam width of $\theta_{-3dB} \approx 3.0^\circ$ on the across-track. Then, the four ULAs on the along-track can also introduce the array gain and the 2D imaging algorithm can be taken. Furthermore, the total number of receiving elements is 128 which is acceptable and economical in the field of engineering application. The echo just below the carrier can also be received which is different from the SAS directivity, so that the gap problem does not exist. The transducer array is designed and produced following the parameters shown in Figure 1b, which meets the requirement of high-resolution detection and also considers engineering applications and cost. Through the moving of the carrier, we can synthesize a virtual array with the aperture size L. The imaging algorithm we proposed is based on the point by point scanning that the actual positions of the elements should be calculated through the motion parameters from the sensors. The carrier's trajectory is compensated so that the actual time delay between the target and element is obtained.

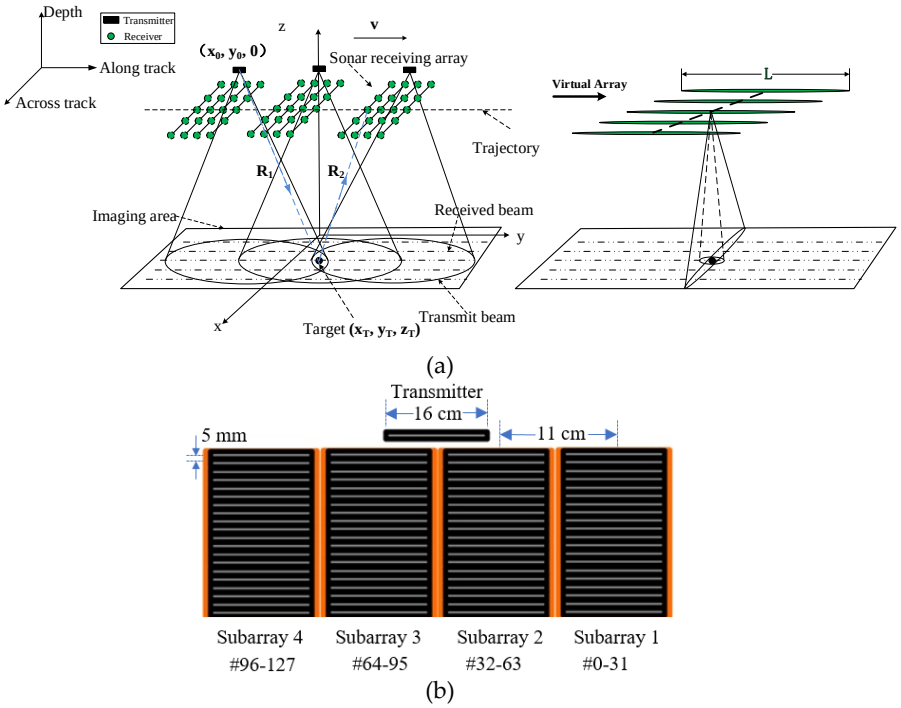

Figure 1. (**a**) Basic echo model of multibeam synthetic aperture sonar (MBSAS). (**b**) Designed 2D MBSAS transducer array.

Normally, the SAS transmitter and receiver are regarded as located at the equivalent phase center (EPC) [18]. However, the 2D MBSAS transducer array locates the transmitter beside the receiving array. Therefore, the range between the transmit position and the scanned area R_1 should be accurately calculated based on the geometric relationships as represented by

$$R_1 = \sqrt{(x_T - x_0)^2 + (y_T - y_0)^2 + {z_T}^2} \tag{1}$$

The transmitter's initial position is $(x_0, y_0, 0)$ and the scanned target is located at (x_T, y_T, z_T). The distance between the receiving element and the scanned area is depicted as R_2 when the carrier moves at the speed of v

$$R_2 = \sqrt{(x_T - x_k(n))^2 + (y_T - y_k(n) - v\tau_k(n))^2 + {z_T}^2} \tag{2}$$

where $(x_k(n), y_k(n), 0)$ is the initial position of the n^{th} element on the k^{th} linear receiving transducer array. Therefore, the carrier's moving time can be indicated as $\tau_k(n)$, which is also the echo time-delay. The acoustic range can be expressed as Equation (3), and the solution expressed in Equation (4) is employed as the time-delay of the back projection (BP) imaging algorithm; c is the acoustic speed.

$$R_1 + R_2 = c\tau_k(n) \tag{3}$$

$$\begin{aligned}\tau_k(n) \quad &= \frac{vy_k(n) - vy_T + c\sqrt{x_0^2 - 2x_0x_T + x_T^2 + y_0^2 - 2y_0y_T + y_T^2 + z_T^2}}{(c^2 - v^2)} \\ &+ \frac{\sqrt{\begin{array}{c}-4\left(c^2 - v^2\right)\left(x_0^2 - x_k^2(n) - 2x_0x_T + 2x_k(n)x_T + y_0^2 - y_k^2(n) - 2y_0y_T + 2y_k(n)y_T\right) \\ +\left(-2vy_k(n) + 2vy_T - 2c\sqrt{x_0^2 - 2x_0x_T + x_T^2 + y_0^2 - 2y_0y_T + y_T^2 + z_T^2}\right)^2\end{array}}}{2(c^2 - v^2)}\end{aligned} \tag{4}$$

The initial element coordinates on the across-track and along-track indicate the transducer array manifold, which is considered in the imaging algorithm of MBSAS. The echoes should be subjected to the preprocessing before the imaging algorithm, including orthogonal transformation to get the analytical signal and pulse compression processing to increase the range resolution. Equation (4) is the analytic solution of the time delay of the transducer array at different synthesized positions, which is a complex process. In actual situations, the transducer array manifold is given and the initial positions can be user-defined so that Equation (4) can be simplified effectively. The transmitting signal is the LFM, which can be expressed as Equation (5) when travel time is t

$$s_t(t) = rect(\frac{t}{T})\exp[j(2\pi f_0 t + \pi u t^2)],\ rect(\frac{t}{T}) = \begin{cases} 1, & |t| \ \leq \frac{1}{2}T \\ 0, & others \end{cases} \tag{5}$$

where f_0 is the initial frequency of the LFM, which lasts for pulse length T. B is the bandwidth of LFM and $\mu = B/T$ represents the chirp rate. The received echo of the selected element after target reflection through travelling time $\tau_k(n)$ can be expressed as Equation (6)

$$s_r(t) = rect(\frac{t - \tau_k(n)}{T})\exp[j(2\pi f_0(t - \tau_k(n)) + \pi u(t - \tau_k(n))^2)] \tag{6}$$

2.2. Processing Scheme of the MBSAS Imaging System

The processing scheme is divided into four steps: orthogonal transformation, pulse compression, synthetic processing on the along-track, and beamforming processing on the across-track, and the first two steps are taken as preprocessing. The echo received by the receiver is converted to an analytical signal through orthogonal transformation. The LFM signal is compressed through the matched filter which obtains the processing gain. The main limit condition of the SAS processing on the along-track

is that the target should be illuminated at least on the edge of each footprint as shown in Figure 1a. The echo coherence must be guaranteed that we should take the SAS processing in a single synthesized aperture period. The receivers of the designed 2D transducer array are separated into 32 subarrays, and each subarray has 4 elements on the along-track. Synthetic processing on the along-track is done in each subarray, generating a virtual 1D ULA that has 32 elements on the across-track. The processing scheme of MBSAS imaging system is shown in Figure 2.

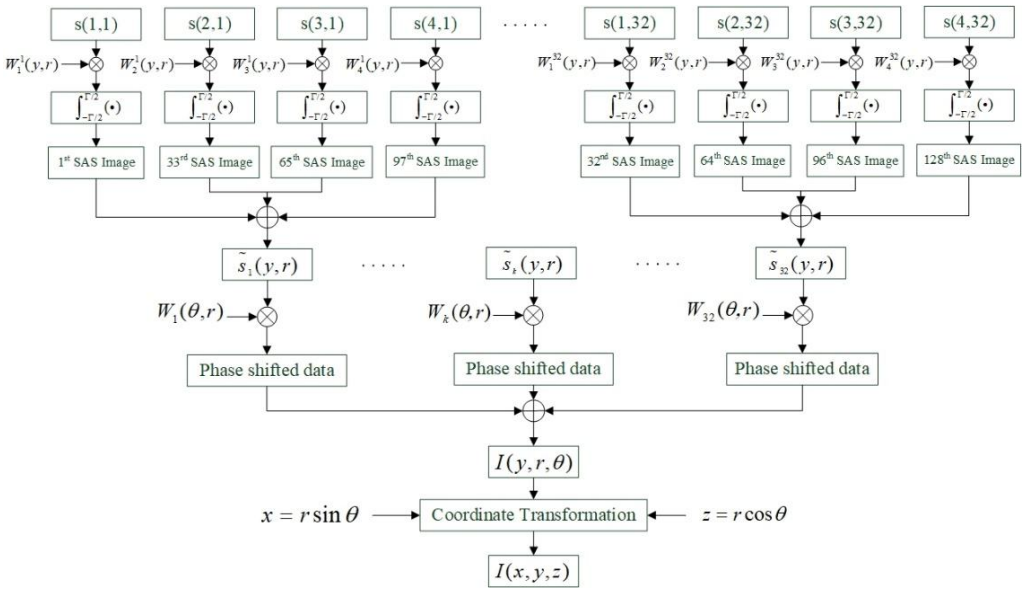

Figure 2. Processing scheme of MBSAS imaging system.

As shown in Figure 2, a complex weighting process is conducted on the analytical signal, which is similar to DFT processing. An integral operation is taken in the whole synthetic aperture period and each element achieves a 2D SAS image. The weight $W_k^n(y,r)$ is calculated through the time delay between the transmitter and the receiver considering the position of the elements, the moving speed and the scanned points, as Equation (4). A weighted summation is taken by each subarray and a virtual element is obtained. Therefore, a ULA similar to an MBES is generated so that the beamforming process can be conducted. Phase shift beamforming then takes place, which employs the near-field model that considers spherical wave propagation. The weight is calculated through the preset beam angle and the range. A weighted summation of the phase shifted data is performed on the 32 elements, and a 3D MBSAS image is obtained which indicates the coordinate system of $y - r - \theta$. The 3D image can also be transmitted to the Cartesian coordinate system through the relationship between distance and beam angle.

2.3. Grating Lobe Problem of MBSAS

Moving speed of the carrier is an important working parameter of SAS that limits the surveying efficiency of the carrier. In the theory of SAS, the max range determines the moving speed as the detected target has to be illuminated on the edge of the footprint at least. That means we take the SAS processing in a single synthesized aperture period. More times the echo synthesizes in a single period, the better the imaging performance which can be obtained, but this lowers the carrier moving speed limit at the same time. The sampling interval, which also limits the moving speed of the carrier, is an important working parameter in engineering applications. According to the sampling theory in 3D space, when the sampling interval exceeds half the size of the transmitter, the grating lobe appears. The grating lobe introduces false targets, decreases the SNR, and is harmful to target recognition. Therefore, the grating lobe problem limits the moving speed and the detection efficiency. As shown in

Figure 3a, the single-element SAS system has no grating lobe problem and indicates the single point target accurately at a sampling interval of 0.5D, where D is the real transmitter aperture size. When the sampling interval reaches 2.0D, false peaks appear and the actual target cannot be recognized. Therefore, we need to analyze the grating lobe problem of MBSAS and provide a method to improve the moving speed of the carrier that meet the actual engineering applications.

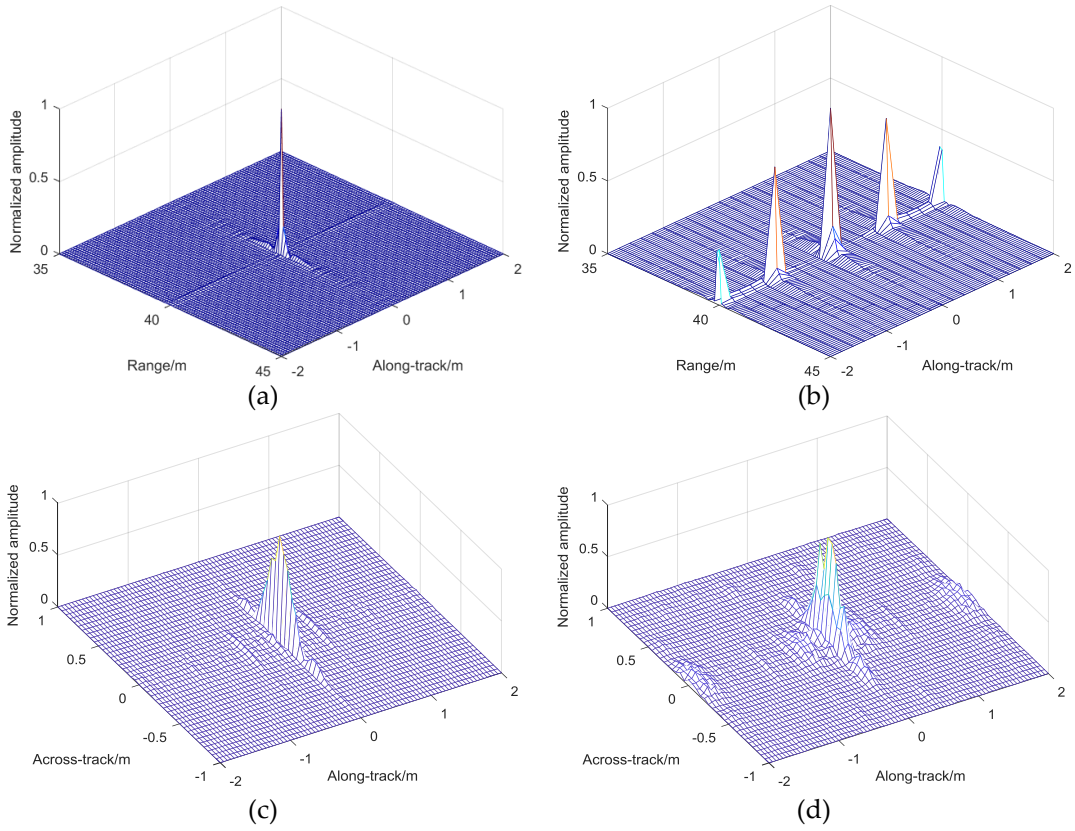

Figure 3. Grating lobe comparison between sampling intervals: (**a**) grating lobe of single element at sampling interval of 0.5D; (**b**) grating lobe of single element at sampling interval of 2.0D; (**c**) grating lobe of MBSAS at sampling interval of 0.5D; (**d**) grating lobe of MBSAS at sampling interval of equivalent value 5.0D.

The restrictive condition of the sampling interval limits the moving speed of the carrier, which also reduces the detection efficiency. For example, when the transmitter aperture size is 16 cm, the moving speed that guarantees a strict sampling interval of 0.5D is just 8 cm/s. The low moving speed is not acceptable in actual applications. The multiple receivers on the across-track can alleviate the grating lobe problem to some extent by coherent accumulation.

Three methods can be employed to overcome such a situation. The first is to improve the pulse repetition frequency (PRF), also called the ping rate in the field of MBES. When the moving speed is limited, the higher the ping rate, the less equivalent the sampling interval. Many kinds of mature MBESs can achieve a ping rate up to 50 Hz, such as the SeaBat 7125, EM 2040, and SeaBat T50P. High ping rate detection reduces the sampling interval equivalently so that we can increase the moving speed of the carrier. As shown in Figure 3d, we simulated carrier moves at a speed of 1.6 m/s and a ping rate of 2 Hz, which indicates that the equivalent sampling interval is 5.0 D. The imaging result in the whole space is acceptable and the grating lobe level increases slightly compared with Figure 3c. However, the high ping rate limits the maximum detection distance, because echoes must be received and coherently accumulated at each synthesized position.

The second way to manage the grating lobe problem is to place multiple elements on the along-track. MBSAS is designed based on the structure of MBES, for which we designed a 2D transducer array to increase the sampling interval. Multiple elements on the along-track can manage the grating lobe problem as each individual ULA can receive an echo in a narrow scope below the array, which equates to increasing the spatial sampling density on the along-track. Multiple elements on the along-track also introduce array gain, some 2D beamforming and subarray processing algorithms can also be taken to improve the imaging performance of MBSAS system.

Sidelobe and grating lobe are suppressed according to the coherent accumulation, which is similar to spatial gain. We compared the synthetic aperture processing output between the single-line and multi-line ULA, which are sliced on the along-track (Figure 4). It is obvious in Figure 4a that the sidelobe and grating lobe levels seriously increase, together with the sampling interval. When the sampling interval reaches 10 times the real transmitter aperture size, a serious false peak problem appears. The multiple elements set in Figure 4b improve the situation so that the false peaks can be managed effectively. However, the problem cannot be thoroughly solved just by adding elements on the along-track considering the system complexity.

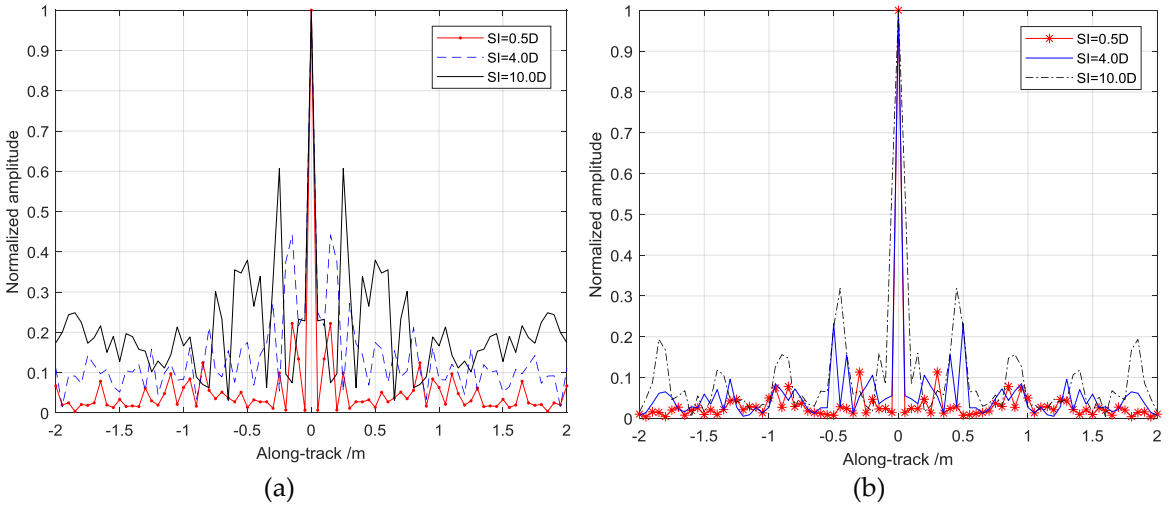

Figure 4. Side lobe comparison between single-line and multi-line receiving array systems. (**a**) Side lobe of single-line array; and (**b**) multi-line array at different sampling intervals.

The third choice to manage the grating lobe problem is to increase the signal bandwidth, which is also called the low-quality factor method. LFM signal is employed in the MBSAS system so that the SNR and detecting distance can be improved effectively. Figure 5a–c compares the imaging output of the 2D transducer array designed as above with a single point target, where the quality factors are Q = 15, 5, and 3.75. The 3D image is sliced on the same depth plane which not only indicates the grating lobe on the along-track but also shows the sidelobe level on the across-track. It is obvious from the comparison that increasing Q can help to manage the grating lobe and side lobe problem. However, with Q increasing as sliced, shown in Figure 5d, the main lobe level reaches the limit value. Moreover, in engineering applications, the wideband transducer array is difficult to design and produce at low cost.

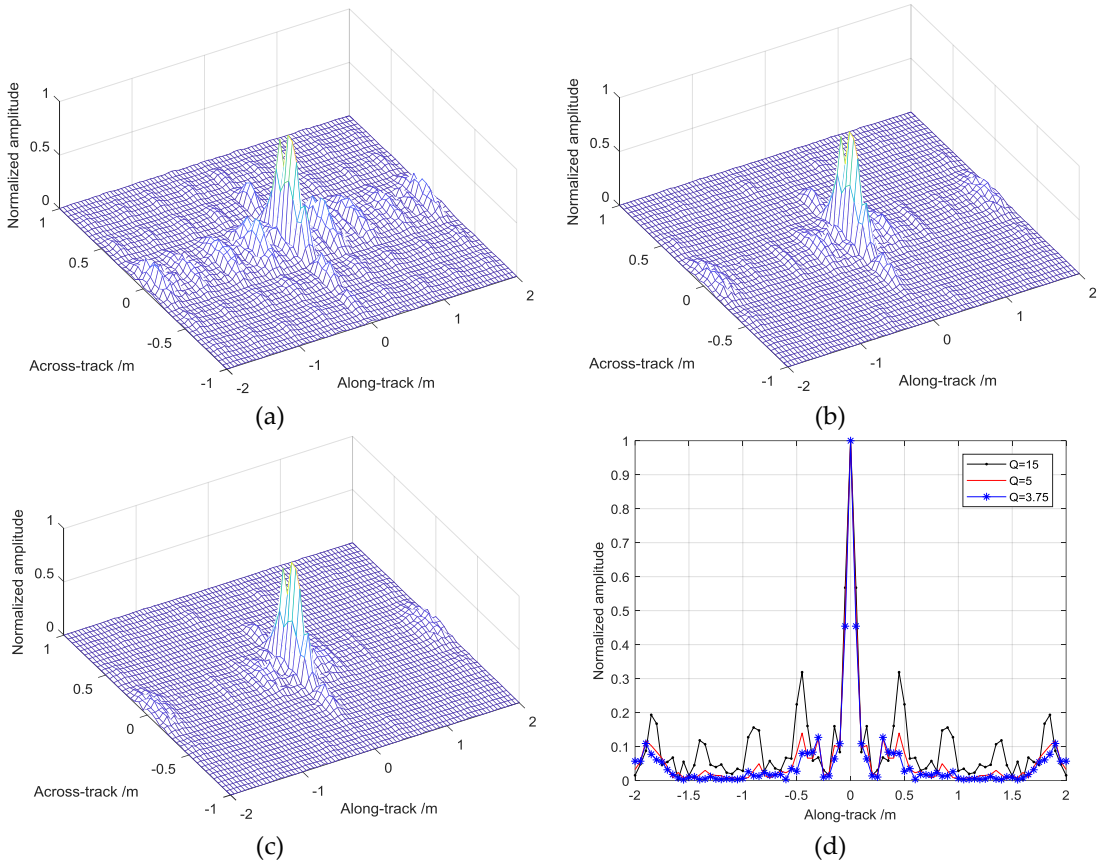

Figure 5. Side lobe comparison between signal bandwidth situations: (**a**) MBSAS output 2D sliced when Q = 15; (**b**) when Q = 5; (**c**) when Q = 3.75; (**d**) MBSAS output sliced on the along-track.

The grating lobe problem is not solved thoroughly, limited by the system complexity and cost, especially in actual engineering applications. Therefore, we have to compromise in this situation to meet the actual requirements. As the grating lobe appears at a certain distance and beam angle from the transducer array center, we can only take the MBSAS processing in a narrow area just below the array to avoid the problem. A whole detecting image can be achieved by moving the carrier so that the image can be stitched together, which is a common method in the MBES imaging field. In summary, we designed the processing scheme of the MBSAS which employs the wideband signal and the 2D transducer array to manage the grating lobe problem. The multi-ping method and image mosaic also help to improve the sampling interval and detection efficiency to meet actual engineering application requirements.

3. Target Simulation and Imaging Algorithm

Target simulation is the basic and necessary work of MBSAS modeling. To provide a detailed echo signal to the imaging algorithm, not only the target main body but also the shadows at different synthetic positions should be simulated in detail. An acoustic highlights model is employed to carry the complex target echo simulation. Furthermore, an imaging algorithm is proposed to demonstrate the feasibility of the 2D MBSAS model.

3.1. Target with Shadow Simulation Approach

The basic unit of target simulation is the single highlight, which is widely employed to evaluate the performance of a detection algorithm, such as received beam angle width and sidelobe level [19]. Thus, the solid target is divided into dozens of highlights through the tangents, as shown in Figure 6a.

Highlights on the surface contribute to the echo accumulated on the elements, ignoring the penetration of the echo. Movement of the 2D transducer array is more complex than the SAS which has single-element or multiple receivers on the along-track. The carrier should move as a uniform rectilinear motion in theory, but an ideal trajectory cannot always be maintained that the motion error must be estimated and compensated. The MBSAS can be equipped by surface vessel or AUV that the high accuracy motion sensors (USBL, DVL, and compass) or motion estimation algorithms based on the echo (DPC and PGA) are employed to calculate the position of each element, considering different application scenarios [20].

The carrier has six dimensional motion parameters, which can be separated by position (sway, surge, and heave) and motion (yaw, roll, and pitch), as shown in Figure 6b. Assuming that the 2D array has M ULAs on the along-track and each ULA has N elements on the across-track, the array we designed has a 4×32 manifold.

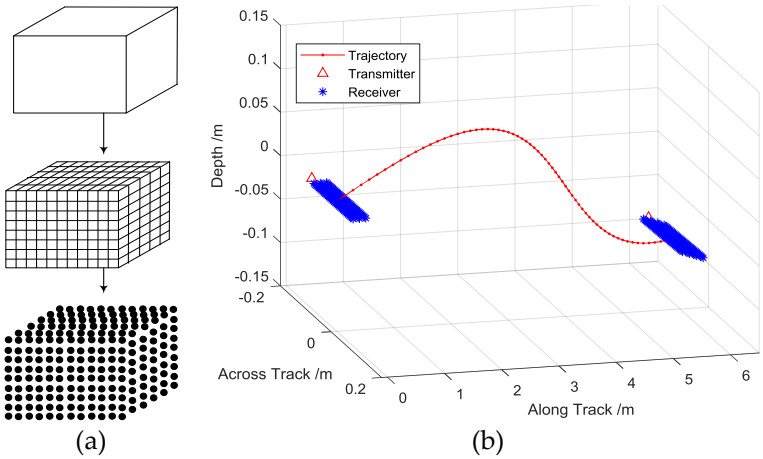

Figure 6. Target segmentation and moving trajectory of carrier: (**a**) highlights segmented on the surface; (**b**) moving trajectory of the carrier.

The coordinates of each element should be calculated accurately according to position and motion parameters to guarantee the validity of the imaging algorithm. We define the rotation angle along the x-axis, y-axis, and z-axis as $[\alpha, \beta, \gamma]$, respectively, then the rotation matrix $\mathbf{M}_\alpha$, $\mathbf{N}_\beta$, $\mathbf{Q}_\gamma$ can be expressed as Equation (7)

$$\mathbf{M}_\alpha = \begin{bmatrix} 1 & 0 & 0 \\ 0 & \cos\alpha & -\sin\alpha \\ 0 & \sin\alpha & \cos\alpha \end{bmatrix} \mathbf{N}_\beta = \begin{bmatrix} \cos\beta & 0 & \sin\beta \\ 0 & 1 & 0 \\ -\sin\beta & 0 & \cos\beta \end{bmatrix} \mathbf{Q}_\varphi = \begin{bmatrix} \cos\varphi & -\sin\varphi & 0 \\ \sin\varphi & \cos\varphi & 0 \\ 0 & 0 & 1 \end{bmatrix} \tag{7}$$

Assuming the carrier's translation along the x-axis, y-axis, and z-axis is Δx, Δy, Δz, respectively, the translation matrix can be defined as $\mathbf{P}_\Delta = [\Delta\mathbf{x}; \Delta\mathbf{y}; \Delta\mathbf{z}]$, where $\Delta(\cdot)$ is the spanned $1 \times MN$ vector. The positions of the receiving elements $\mathbf{P}_{r1}$ can be calculated through the rotation matrix and translation matrix from the initial position $\mathbf{P}_{r0}$ as Equation (8)

$$\mathbf{P}_{r1} = \mathbf{M}_\alpha \mathbf{N}_\beta \mathbf{Q}_\varphi \mathbf{P}_{r0} + \mathbf{P}_\Delta \tag{8}$$

Similarly, the transmitter's position can be calculated through Equation (9).

$$\mathbf{P}_{T1} = \mathbf{M}_\alpha \mathbf{N}_\beta \mathbf{Q}_\varphi \mathbf{P}_{T0} + \mathbf{P}_\Delta \tag{9}$$

In the simulation of the target, the shadows area is an important factor that also indicates the characteristics of the target. We employ the normal vector of the surface to calculate the shadow area of

the target. Any plane in the 3D space can be described by the point normal equation. The surface of the target contributes to the signal when it is illuminated by the transmitted echo. When the included angle between the normal vector and the connection from the transmitter to the surface is an obtuse angle, this surface contributes to the received signal. The normal vector Figure 7a shows that each surface has its own normal vector and the bottom is never illuminated. The normal vector of the surface can be expressed as $\vec{\mathbf{n}} = (A, B, C)$, which is vertical to the plane. Given a certain point $M_0 = (x_0, y_0, z_0)$ on the surface, any point on the surface $M = (x, y, z)$ has the limit as $\vec{\mathbf{n}} \perp \vec{MM_0}$, which is also calculated as Equation (10).

$$\vec{\mathbf{n}} \cdot \vec{MM_0} = A(x - x_0) + B(y - y_0) + C(z - z_0) = 0 \tag{10}$$

The included angle between the target surface and the coordinate system plane can be expressed as Equation (11)

$$\cos\theta = \frac{\left|\vec{\mathbf{m}} \cdot \vec{\mathbf{n}}\right|}{\left|\vec{\mathbf{m}}\right| \cdot \left|\vec{\mathbf{n}}\right|} \tag{11}$$

where $\vec{\mathbf{m}}$ is the normal vector of each coordinate plane, such as $\vec{\mathbf{m}}_{x,y} = (0, 0, 1)$, $\vec{\mathbf{m}}_{y,z} = (1, 0, 0)$, $\vec{\mathbf{m}}_{x,z} = (0, 1, 0)$.

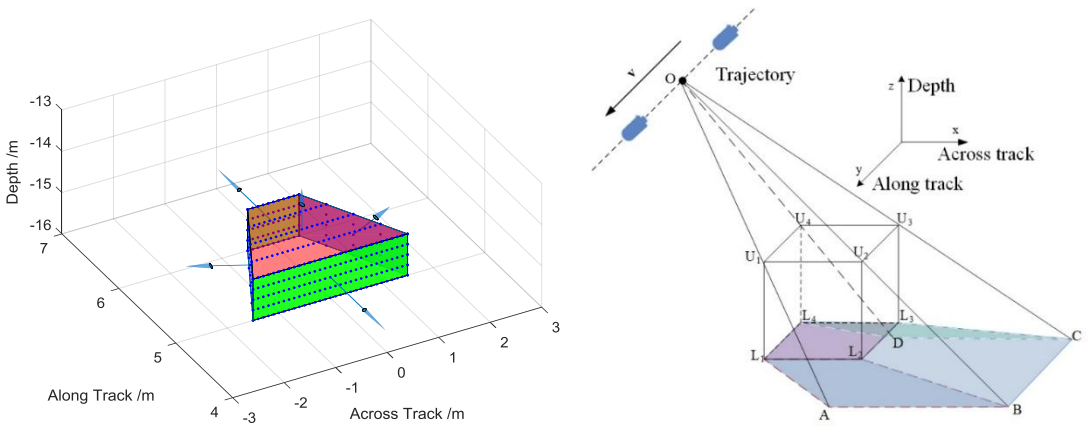

Figure 7. Target simulation model: (**a**) normal vector of target surface; (**b**) shadow area of target calculated from the carrier position.

The target echo shadow area is delineated through the line connecting the transmit position O and the seabed as shown in Figure 7b. The points U_1–U_4 are the top vertices of the target and points L_1–L_4 are the bottom vertices. Points A–D are subpoints of O that connect the top vertices and seabed. The shadow area is defined by the linear function $l(\cdot)$, which connects the transmit position O and the vertices, together with the seabed. Furthermore, when the target is located on the seabed, the bottom side also cannot contribute to the returned echo. The shadow area can be analytically described according to the connection between the sampling position and the vertices of the target. We define the plane equation of side $U_4L_4L_3U_3$ as $y = y_1$ and that of side $U_1L_1L_2U_2$ as $y = y_2$, where y_1 and y_2 are constant to indicate the location of the target. The connection between the vertices and the origin varies with different synthetic positions and forms different shadow areas, described by Equation (12). The synthetic shadow area after imaging is the intersection of the shadow areas formed at each sampling position, which is smaller than a single-position shadow

$$\begin{cases} l_{L_1A} < 0 \& l_{AB} < 0 \& l_{BC} < 0 \& l_{CL_3} < 0 \& l_{L_3L_4} < 0 \& l_{L_4L_1} < 0, vt < y_1 \\ l_{L_1A} < 0 \& l_{AB} < 0 \& l_{BC} < 0 \& l_{CD} < 0 \& l_{DL_4} < 0 \& l_{L_4L_1} < 0, y_1 < vt < y_2 \\ l_{L_1L_2} < 0 \& l_{L_2B} < 0 \& l_{BC} < 0 \& l_{CD} < 0 \& l_{DL_4} < 0 \& l_{L_4L_1} < 0, vt > y_2 \end{cases} \tag{12}$$

3.2. Imaging Algorithm for 2D MBSAS

SAS imaging theory separates the detection area into different pixel points. The time delay between the pixel points and the elements is compensated and the echoes accumulate coherently according to the array manifold. The 2D SAS image of the detection area, which only indicates the azimuth and range direction, can be obtained intuitively [21]. Single-element SAS processing is first performed on the along-track. After that, the multi-element SAS signals are coherently accumulated to convert the multiple elements to a virtual single element. SAS processing of the received echo in the element space is undertaken to obtain the 2D SAS image according to Equation (13), where the center of the virtual array is the origin coordinates

$$I(\vec{r}) = \frac{1}{\Gamma}\int_{\Gamma/2}^{-\Gamma/2} s_r(t_d(t;\vec{r})),t)\exp(j2\pi f_0 t_d(t;\vec{r}))dt \tag{13}$$

where $t_d(t,\vec{r}_T) = 2\left|\vec{r}(t) - \vec{r}_T\right|/c$ is the time-delay of the SAS echo, which is the vector expression of $\tau_k(n)$; and $\vec{r}(t)$ is the vector of the carrier and $\vec{r}_T$ is the vector of the target, which is processed in the synthetic aperture period Γ. $\vec{r}(t)$ is the analytic vector in the 3D space and performs scalar in the range and time delay as r. The center frequency of the echo is expressed as f_0, and B is the bandwidth of the LFM echo. The single-element imaging output of SAS processing is shown in Equation (14), which has been solved analytically [22]

$$I(y,r) = \sin c(\frac{2f_0}{c}\frac{(y-y_T)v\Gamma}{\sqrt{(y-y_T)^2+r^2}})\cdot\sin c(\frac{2B}{c}(r-r_T))\cdot\exp(j\frac{4\pi f_0}{c}(r-r_T)) \tag{14}$$

After traversing all the elements, the 2D transducer array is converted to a virtual ULA on the across-track, which is similar to a conventional MBES system. On the across-track, beamforming is conducted to estimate the echo direction of arrival (DOA). The full-scan 3D imaging result is achieved as Equation (15), and the Taylor expansion is employed to simplify the formula

$$\begin{aligned} II(y,r,\theta) = \sum_{n=0}^{N-1} I(y,r+c\tau(n),n) \approx \sin c(\tfrac{2f_0}{c}\tfrac{(y-y_T)v\Gamma}{\sqrt{(y-y_T)^2+r^2}})\cdot\sin c(\tfrac{2B}{c}(r-r_T))\cdot\tfrac{\sin(\frac{2N\pi d_x}{\lambda}(\sin\theta-\sin\theta_T))}{\sin(\frac{2\pi d_x}{\lambda}(\sin\theta-\sin\theta_T))} \\ \cdot\exp(j(\tfrac{4\pi}{\lambda}(r-r_T)+\tfrac{(N-1)\pi d_x(\sin\theta-\sin\theta_T)}{\lambda})) \end{aligned} \tag{15}$$

where $\tau(n) = \sin\theta\cdot nd/c$ is the n^{th} time delay of the element. The average element spacing d_x and the number of elements N indicates the manifold of the designed transducer array; λ is the wavelength of the echo, and $d = \lambda/2$ as designed; and θ is the preset beam angle and θ_T is the beam angle of the target. In the theory of sonar imaging, when the scanned point matches the target position, the echoes superpose most effectively. It is also shown in Equation (15) that the imaging output $II(y,r,\theta)$ is maximum when $y = y_T, r = r_T, \theta = \theta_T$. The output is the 3D image under the coordinates of $y-r-\theta$, which is not obvious for detection. The image should be transmitted to the coordinates of $x-y-z$ to produce the echo image on the across-track and along-track, and the depth direction. The image points are transmitted uniformly according to $x = r\sin\theta, z = r\cos\theta$.

MBSAS images show the energy output in 3D space, while in actual situations, we pay more attention to detecting of the time of arrival (TOA) of the preformed angles. Accurate TOA estimated from noised echoes is also the thinning of the detailed sonar image. Target detection plays a more important role in the field of engineering [23]. The output of MBSAS beamforming contains phase information that could be employed for TOA estimation. General energy-based detection methods such as weighted mean time (WMT) and phase difference methods such as the split beam and multi-subarray (MSA) algorithms can also be introduced in MBSAS detection theory, which is similar to the MBES detection system [24,25].

3.3. Simulation

To evaluate the performance of the MBSAS modeling and the imaging algorithm, simulations are undertaken according to the echo model we designed in Figure 1. First, plane targets are simulated. We locate dozens of independent highlights on the same depth plane, which can more directly indicate the performance of the MBSAS imaging algorithm, especially on the along-track. The main parameters are shown in Table 1. A virtual receiving array with an aperture of 4 m is generated through the processing. The across-track is defined as the direction of x and the along-track as y.

Table 1. Transducer array and target parameters

Parameter	Value
Echo frequency	150 kHz
Signal bandwidth	20 kHz
Pulse width	10 ms
Depth	10 m
Highlight spacing	15 cm

Figure 8 compares different imaging results. The trajectory and position of the element are shown in Figure 8a, showing that we locate 25 highlights on the same depth plane with 15 cm spacing. Different imaging algorithms are used to compare the results. Figure 8b shows the SAS imaging result, with the same number of elements, which can separate the target location on the along-track. However, the SAS theory can only obtain the 2D image, so that the actual location on the across-track is replaced with range. Moreover, the size of the target on the along-track is seriously distorted with a reduced energy focusing ability. Figure 8c indicates that the aliasing problem damaged the validity of the imaging result obtained via MBES, which was defocused seriously on the along-track. Moreover, the energy leaking to the side lobe also affected the beamforming processing on the across-track. Although the targets can be separated, false peaks appear and the energy focusing ability decreases seriously. The number of targets and locations of highlights are mixed. For comparison, the imaging result obtained via MBSAS is shown in Figure 8d. The targets can be separated on the along-track with constant resolution. Beamforming on the across-track achieves the same resolution as MBES, which also recognizes the targets. MBSAS also achieves higher energy focusing ability, owing to more echo superposition.

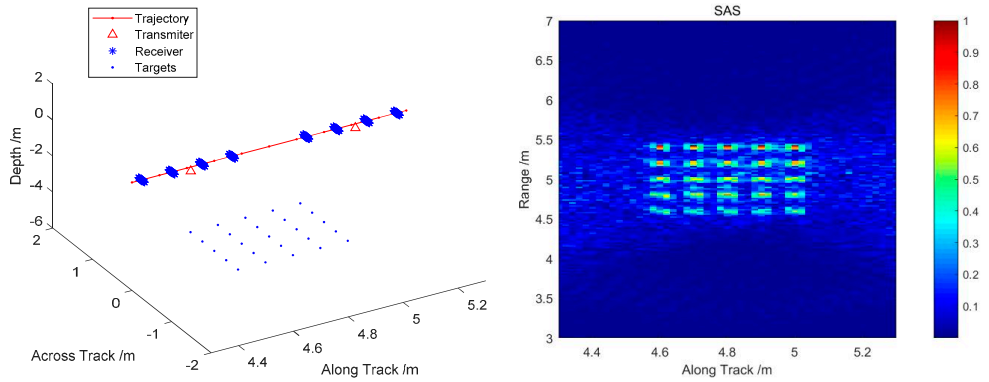

(a) (b)

Figure 8. *Cont.*

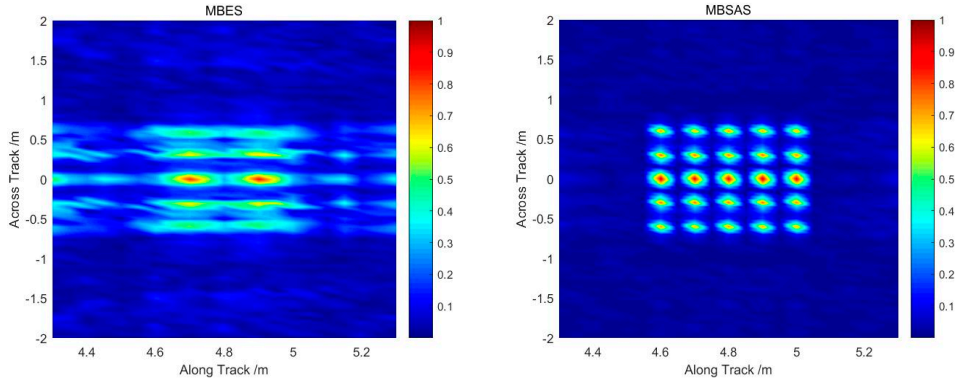

Figure 8. Comparison between imaging algorithms: (**a**) target set and position of carrier; (**b**) imaging result via SAS algorithm; (**c**) imaging result via MBES algorithm; (**d**) imaging result via MBSAS algorithm.

The image above is also sliced and shown on the across-track and along-track to observe the resolution. The beamforming on the along-track of MBSAS is similar to that of MBES, so we can evaluate the results under one angle coordinate. The SAS image is under the coordinates of $y - r$, which cannot be compared with the MBES and MBSAS system on the across-track. Figure 9a indicates that even if the targets can be separated by MBES on the across-track, some false peaks appear. The sidelobe levels were damaged by the mixed echo from the along-track. MBSAS imaging reveals the beam width of the array and separates the multiple targets by θ_{-3dB}, which has the same target resolution on the across-track as conventional MBES. The resolution on the along-track of MBSAS does not vary with the beam angle, and we focus more on the constant resolution in engineering situations. Therefore, the imaging resolution on the along-track is sliced under Cartesian coordinates. It is shown in Figure 9b that the resolution of MBES decreases substantially with increasing beam angle and cannot easily separate the multiple targets. SAS imaging has constant resolution on the along-track that can separate the targets. However, the SAS has a low ability to estimate the DOA on the across-track, so that the mixed echo reduces the sidelobe level of the image. The MBSAS imaging is slice performed with constant high resolution, which has the same ability as SAS. The multiple targets can be separated clearly with high energy focusing ability, given the narrow main lobe width and low sidelobe level.

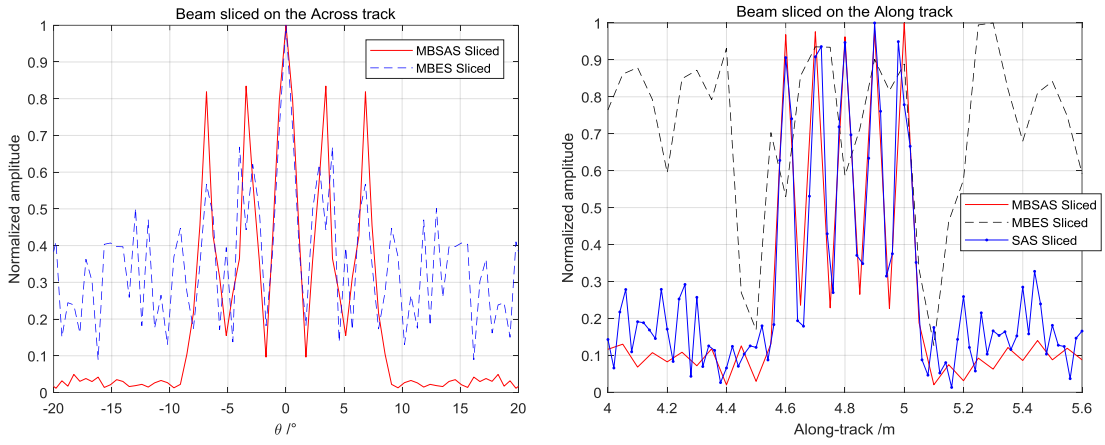

Figure 9. Comparison of sliced imaging output: resolution on (**a**) the across-track and (**b**) the along-track.

After that, a solid target is simulated to evaluate the performance of different imaging algorithms in the 3D space. Assuming that there is a solid target located in a detection area divided into hundreds of highlights, and the distance between the highlights is 0.3 m on the across-track, 0.1 m on the

along-track, and 0.2 m in the depth direction, there are 125 echo highlights located in the detection area. To evaluate the validity of the model, the target is first briefly simulated while ignoring the shadows and seabed, according to the designed 2D MBSAS model and the referred imaging theory. The imaging result is the full 3D detection of the scanned area. Therefore, the sonar image is prospectively sliced to evaluate the performance of the MBSAS imaging algorithm. The simulation parameters are listed in Table 2.

Table 2. Transducer array and cube target parameters.

Parameter	Value
Echo frequency	150 kHz
Signal bandwidth	20 kHz
Pulse width	10 ms
Target size (x, y, z)	1.2 m × 0.4 m × 0.8 m
Target separation distance (x, y, z)	30 cm × 10 cm × 20 cm

Figure 10a shows the image achieved by the MBES imaging algorithm. The positions and number of targets on the along-track cannot be identified, as such detection is limited by the beam footprint. Moreover, due to echo aliasing throughout the whole space, the sliced perspective image is severely defocused, which introduces false targets. Figure 10b indicates the image achieved by the MBSAS imaging algorithm. The targets can be effectively recognized with high contrast. The image slices show that the targets can also be identified in detail in 3D space, as shown. Targets located at the vertical bottom area can still be detected, rather than detecting gaps as in the SAS image. Moreover, the MBSAS image has a better echo energy focusing ability than MBES, owing to the array gain of the 2D planar transducer array. The simulation results indicate that the model and the imaging algorithm of MBSAS can effectively improve the resolution of MBES without gaps.

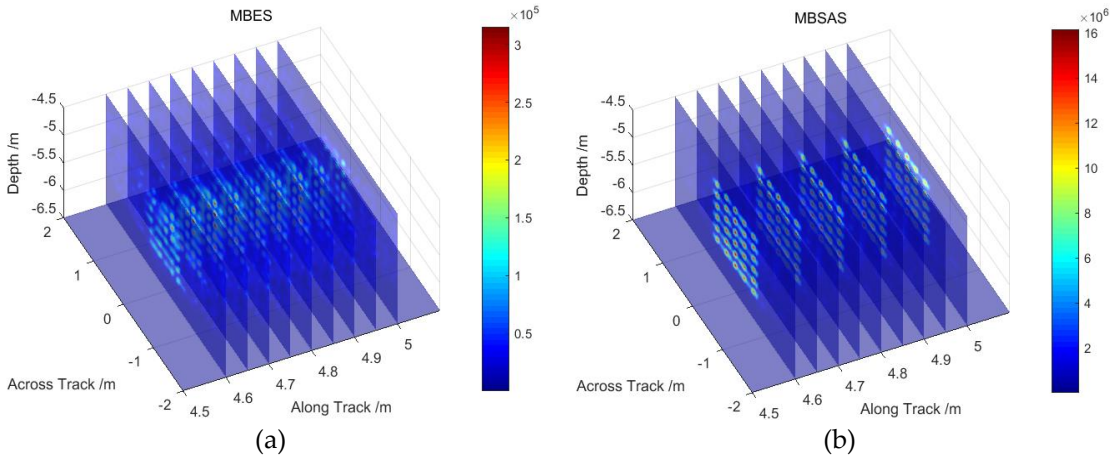

Figure 10. Comparison of 3D imaging algorithms: sliced view of (**a**) MBES image and (**b**) MBSAS image.

To evaluate the performance of the modeling of targets with shadows, a detailed simulation is conducted under the parameters shown in Table 3. A cube target is located on the seabed with a shadow area. The echo signal is accumulated in the 2D transducer array according to the designed array manifold and the synthetic position. MBSAS imaging and target detection based on the phase difference method are undertaken.

Table 3. Simulation parameters for target with shadows.

Parameter	Value
Target size (x, y, z)	2 m × 0.8 m × 2 m
Target separation distance (x, y, z)	0.1 m × 0.1 m × 0.1 m
Seabed separation distance (x, y)	0.2 m × 0.4 m
Cube center location (x, y, z)	(5, 2, –9)
Synthetic aperture size	4 m

The target highlights and shadow area are simulated, where the shadows vary as the transducer array sails along the trajectory. The target obstructs the echo and forms the shadows area on the designed seabed. The shadow area forms according to the line connecting the transmit position and the seabed at different view positions, as shown in Figure 11a–c. The shadow area has center symmetry on the whole moving trajectory. The synthetic shadows area is the intersection of the shadows formed at each sampling position and is smaller than a single-position shadow. The synthetic shadow area is constant and does not change with the sampling position, which can effectively demonstrate the location of the target. The synthetic shadow shown in Figure 11d is smaller than a single-position shadow area. The carrier moving trajectory and the location of the receiving elements at different sampling moments are also shown in the figure. The center of the array is regarded as the origin, which limits the line connecting the transducer array and the seabed.

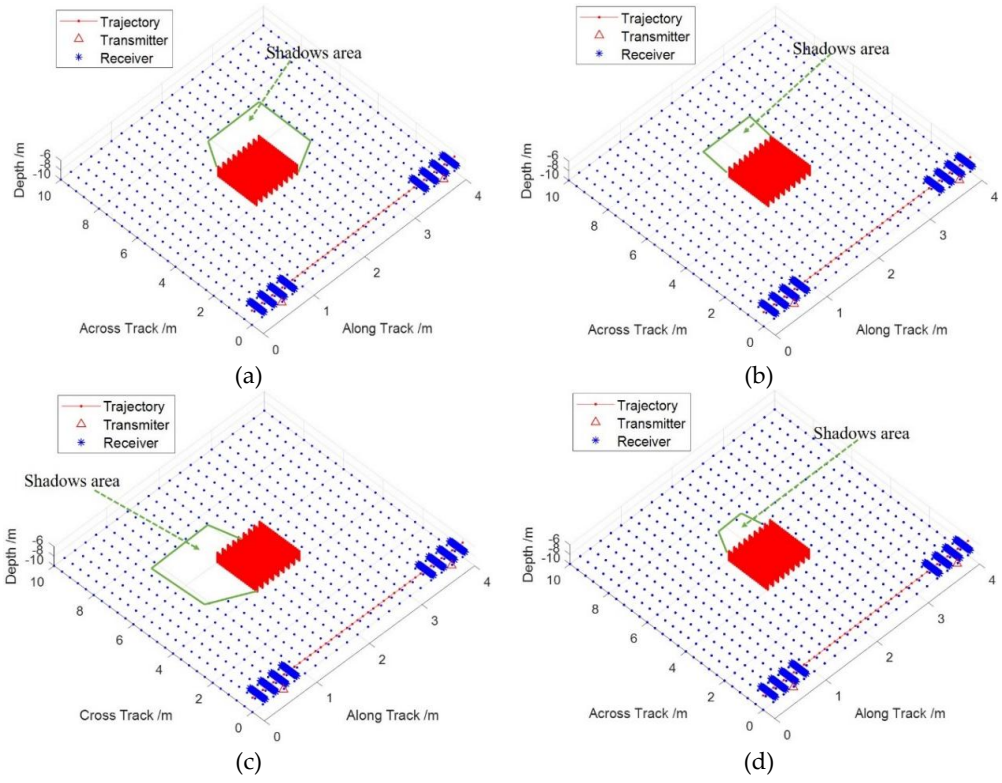

Figure 11. Target and shadow areas at different viewing positions: shadows at the (**a**) start viewing position; (**b**) middle viewing position; (**c**) end viewing position; and (**d**) final synthetic shadow area.

Three cube targets are also simulated to evaluate the performance of distinguishing adjusted targets. We locate the cube targets on both sides and the right bottom of the trajectory. The targets and the shadow area are considered in the model to reveal their mutual influences. The targets are independent of each other, and their positions are parallel and progressive. The image is sliced as shown in Figure 12, where the targets and the shadows are marked.

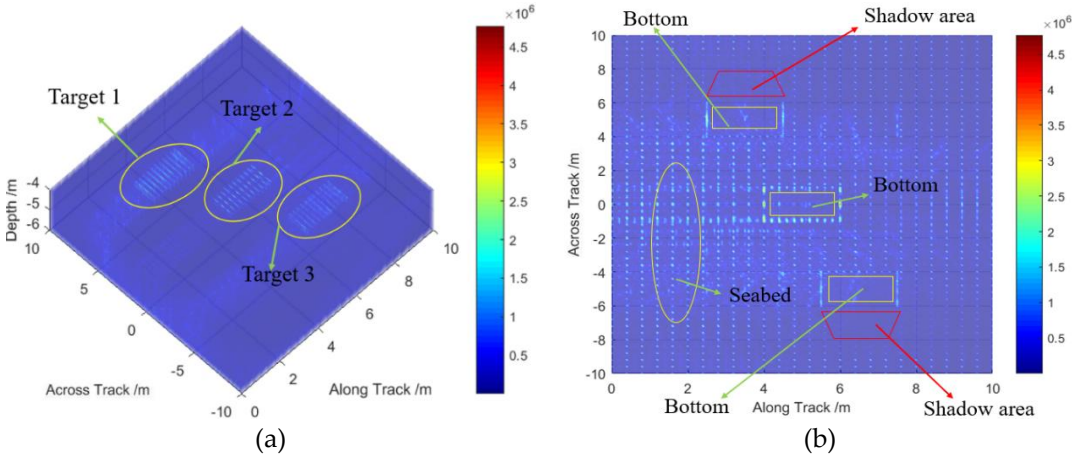

Figure 12. Simulation of three adjusted targets: (**a**) imaging output of the targets; (**b**) perspective-sliced image from the bottom view.

The sliced image is shown in Figure 12a. The adjusted targets can be separated after MBSAS image processing as marked. Then, the 3D image is sliced in the bottom view, which can indicate the shadows and the seabed in more detail. The targets in Figure 12b match the MBSAS imaging result. The seabed and shadows are the same as calculated in Equation (12). The cube bottom on the seabed is not highlighted because the bottom is not illuminated by echoes. Furthermore, the targets directly below the trajectory do not generate shadows, as they are vertically irradiated. The adjusted targets can be recognized effectively with high resolution according to MBSAS theory. It is important to note that, limited by the beam width, the imaging resolution on the across-track inevitably decreases with increasing distance. Therefore, some high-resolution beamforming algorithms used on the across-track, such as minimum variance distortionless response (MVDR) and deconvolved beamforming, should be researched further but are not the focus of this paper [26,27].

4. Instrument Design and Experimental Results

The MBSAS principle prototype was designed and produced to verify the novel theory proposed. The instrument is designed according to the 2D transducer array manifold with 128 sampling channels. Dozens of high-speed operational amplifiers (OAs) and analog to digital converter (ADCs) are employed by FPGA to acquire the echo signal. The total amount of data uploaded to the processing unit is up to 1.15 Gbit/s, owing to the hundreds of elements and a high sampling rate. The data transmission rate is a bottleneck of system application that downsampling and reducing sample length methods are employed to coordinate with the processing unit.

The MBSAS prototype system is shown in Figure 13a, and a control unit is also designed to manage the data and supply the power. The performance of the proposed modeling and imaging algorithm was evaluated through a designed tank experiment. An anechoic tank was employed to undertake the experimental research. The accurate trajectory of the MBSAS transducer array should also be strictly guaranteed. Therefore, a four degree of freedom (DOF) automatic rotation device was employed to move the transducer array to the designed sampling position. The experiment site, MBSAS transducer array, and targets to be detected are shown in Figure 13b.

In this tank experiment, we designed the 2D array to move from −70 cm to 70 cm to synthesize a virtual receiving transducer array whose aperture is equal to 140 cm. The echo in eight sampling positions was synthesized with a step of 20 cm. The main parameters of the echo signal are shown in Table 4.

First, we located a single 13 cm diameter solid ball in the experimental tank. To compare with the resolution of the MBES imaging algorithm, we should locate the target from a long distance. Therefore, the range between the targets and the transducer array was approximately 13 m. Thus, the footprint of the beam on the along-track was approximately 40 cm, which is much larger than the actual size that

the actual target size cannot be recognized. The constant resolution on the along-track of MBSAS was approximately 8 cm, limited by the actual aperture of the transmitter.

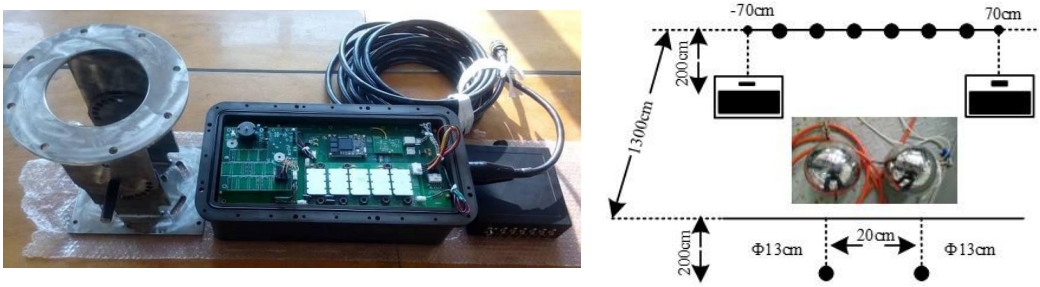

(a) (b)

Figure 13. Experimental site and targets to be detected: (**a**) MBSAS principle prototype used in the experiment; (**b**) experimental site and targets.

Table 4. Main parameters for MBSAS experiment.

Parameter	Value
Echo frequency	150 kHz
Signal bandwidth	20 kHz
Sampling rate	600 kHz
Pulse width	10 ms
Transmitter size	16 cm
Receiver aperture on along-track/across-track	44 cm/16 cm
Detection distance	13 m
Synthetic aperture size	1.4 m

The imaging output in Figure 14 shows that the target is located only in the center beam on the across-track, which is similarly limited by the beam footprint. Therefore, we display the image under the coordinate system of $y - r$. Figure 14a shows the MBES image where the actual size of the target is magnified. The actual position of the preset target is also falsely indicated. The resolution on the along-track decreases substantially with increasing range. Furthermore, echo energy aliasing disturbs the beamforming on the across-track where the false target occurs in the image. As a comparison, Figure 14b shows the MBSAS image indicating the actual size and location of the target. Moreover, the noise is suppressed well, which clears the background of the image. MBSAS also increases the echo energy focusing ability, which is a great benefit to high-resolution sonar.

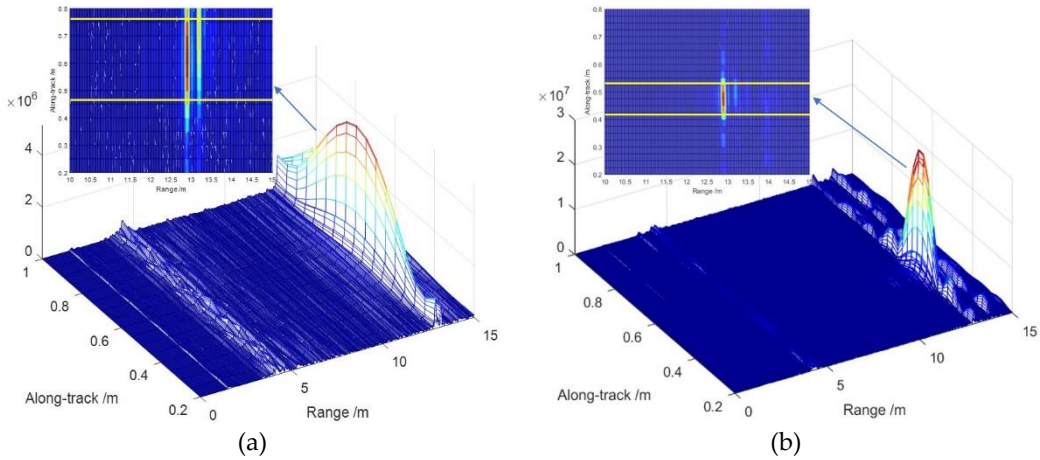

(a) (b)

Figure 14. Imaging output and target size comparison: imaging results from (**a**) MBES of the middle beam, and (**b**) MBSAS of the middle beam.

Second, we located a cube target with a side length of 30 cm in the tank experiment. The imaging result of the conventional side scan sonar system is shown in Figure 15a. Limited by the footprint on the along-track, the actual size of the target cannot be effectively recognized where the echo mixed seriously. The SAS processing is taken as a comparison to identify the actual size of the target on the along-track. In Figure 15b we can see that a peak highlight is obvious in the position where we located the target. The effective echo lasted for a long period on the along-track and some suspected sidelobe peaks appear with a low energy contrast. The imaging result on the along-track can indicate the size of the target through the width of the main lobe. However, the imaging of the side scan sonar and the SAS can only achieve the 2D result, which just indicate the position of the target on the along-track and range direction. The imaging algorithms are also disturbed by the echo from the across-track as the cube target also has an actual size on the across-track. Therefore, we should employ the 3D view image to identify the position and size in the whole space.

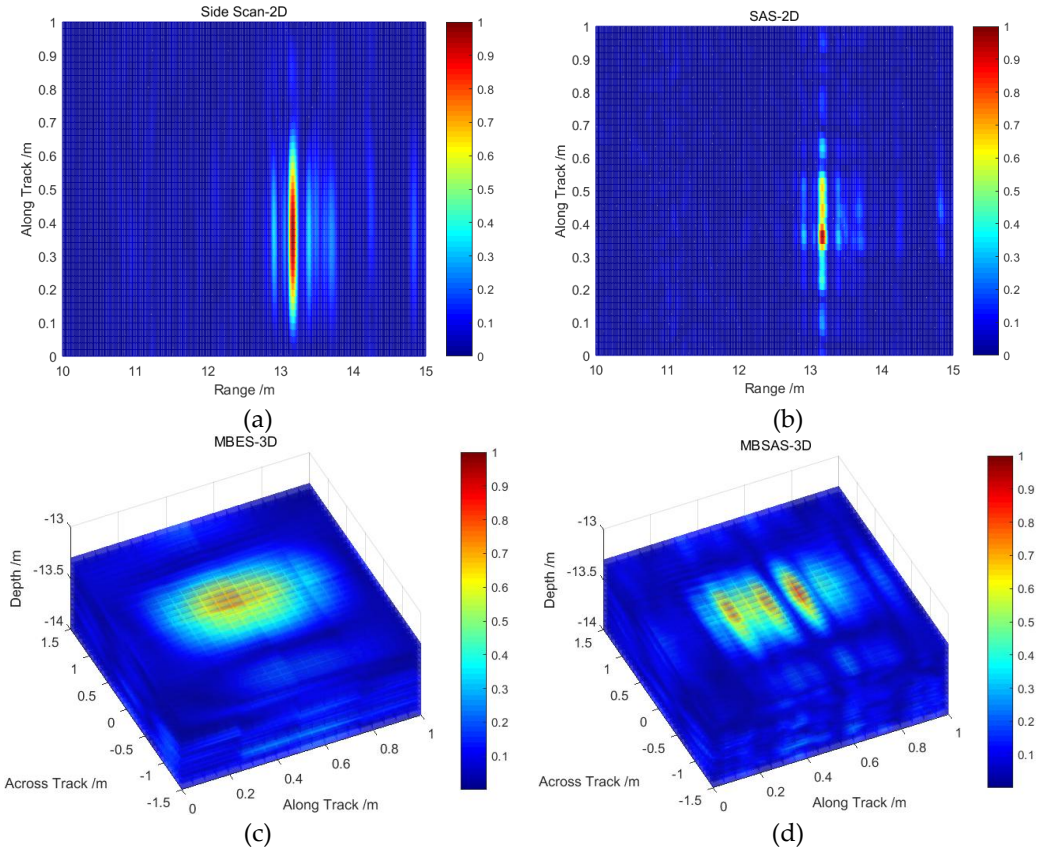

Figure 15. Comparison of imaging algorithms: cube target imaging results via (**a**) side-scan sonar; (**b**) SAS; (**c**) MBES; and (**d**) MBSAS.

The MBES imaging algorithm generates 3D detection in the whole space, as shown in Figure 15c. The 3D image is also sliced in the depth direction to show the resolution on the across-track and along-track. It is obvious that the position is recognized effectively, and the size of the target on the along-track and across-track is larger than the actual one, which is limited by the footprint in the two directions. The beamforming processing can increase the resolution on the along-track, but it is not unlimited. We also employ MBSAS imaging processing to achieve a more detailed result as shown in Figure 15d. Synthetic aperture processing is taken on the along-track and beamforming on the across-track that obtain a 3D detection result. Three highlights appear on the along-track, which indicate not only the position, but also the size of the target with a high energy focusing ability, as the size designed. The echo is separated by the beamforming on the across-track, so that the highlights on the along-track are independent.

To evaluate the ability of MBSAS imaging to separate adjusted targets, dual solid ball targets are located to test the resolution of the imaging algorithm. The diameter of a single ball is 13 cm, and the distance between the sphere centers is 20 cm. The imaging output of MBSAS indicates the positions of the targets in the 3D space. The image is sliced on the top of the target plane to show the detailed resolution of MBSAS. Figure 16a shows the result of MBES imaging, which cannot separate the dual balls, owing to the limit of the beam footprint. Echo aliasing occurs in the beam-space and is difficult to observe in the image. The beam width and sidelobe of the MBES algorithm also disturb the actual shape imaging in the detection area. Figure 16b shows the imaging result of the MBSAS algorithm. Dual balls are separated effectively by actual size with a constant resolution that ignores the beam width and range. Furthermore, the echo energy focusing ability is clearly enhanced.

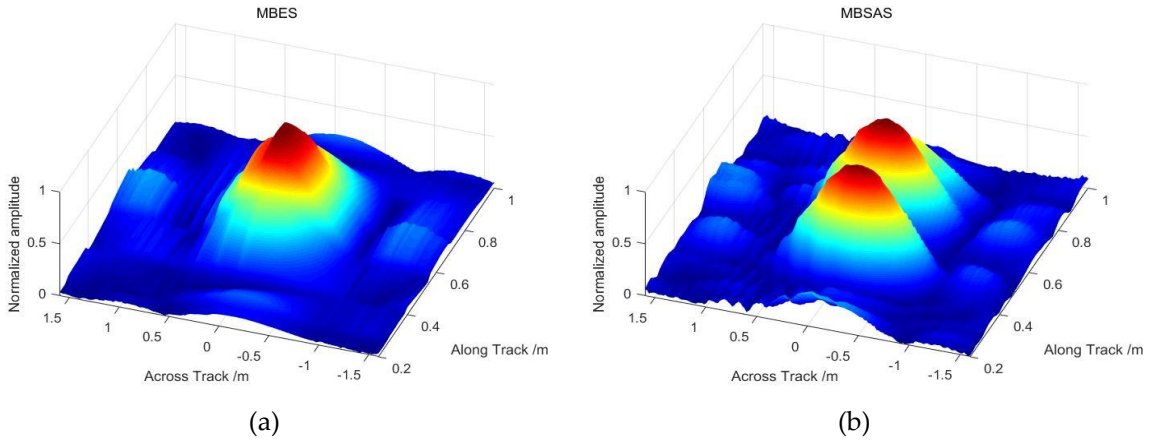

(a) (b)

Figure 16. Comparison of imaging algorithms: dual ball imaging slice of (**a**) MBES and (**b**) MBSAS.

5. Discussion

5.1. Advantages of MBSAS as an Imaging System

MBES and SAS are widely employed as the major imaging sonar systems in the application of cables, unexploded ordnance, seabed mapping, harbor security, and gas detecting. Many mature products have been provided to users, such as Kongsberg EM 2040, RESON SeaBat 7125 (MBES), Kongsberg HISAS 1030, and Kraken AQUAPIX (SAS). Practical technologies have also been proposed to improve the performance of SAS, such as the multi-subarray SAS or interferometric synthetic aperture sonar (InSAS). Nevertheless, limited by the detection principle, shortcomings of the systems are also obvious. SAS systems obtain a constant along-track resolution but have to equip an additional MBES as a gap filler to detect the area just below the carrier, which is limited by the transducer directivity. The accuracy of the height information is lower than MBES, through the fewer elements phase difference or the inversion algorithms. MBES technology is also greatly developed that the detailed images perform a benefit for target surveying, such as the function of water column, dual swath, and snippet side scan. Although MBES can achieve a full-scan image with a high accuracy height estimation, the along-track resolution decreases seriously with the increasing distance.

MBSAS is a novel MBES technology attempting to combine the benefits of MBES and SAS. MBSAS can achieve a 3D full-scan detection without extra gap filler. Dozens or even hundreds of elements on the across-track guarantees high-resolution beamforming and supply the detailed water column image, together with an accurate target depth estimation. Synthetic aperture algorithm processing on the along-track offers a constant resolution as SAS and the 2D transducer array also introduces obvious array gain. Therefore, MBSAS performs a potential device that achieves a 3D full-scan imaging with a high-resolution.

5.2. Foresight and Limiting Condictons of the Application of MBSAS

MBSAS system combines the benefits of MBES and SAS but also partly limited by the theory of them. Especially for the SAS theory, the moving speed of the carrier and the motion estimation and compensation problem inevitably affect the imaging performance. Usually, the moving speed is limited by the max range of the sonar and the target should be illuminated at least on the edge of each footprint. The echo coherence must be guaranteed that we take the SAS processing in a single synthesized aperture period. In the actual applications, we do not need to guarantee no grating lobe at the whole area that we just take the imaging at the narrow area just below the array. The bandwidth of the LFM can also increase the sampling interval on the along-track that the moving speed of the carrier can be improved to meet the engineering applications. Owing to the design of the transducer array and the processing scheme of our MBSAS, we can achieve a 1.6 m/s moving speed of the carrier that meets most applications.

Current MBES can usually be mounted on the surface vessel but can also be carried by AUV with the water-pressure resistance transducer array, such as the SeaBat 7125. MBSAS system can also be equipped by the surface vessel and the AUV system. An ideal moving trajectory cannot always be maintained which is inevitably influenced by wind and waves. Carrier's motion error must be estimated and compensated to manage the image defocusing problem. The surface vessel can supply accurate motion information through the high precision sensors, such as the compass and the aided GPS, also help to improve the correctness of the motion parameters. The accuracy of the sensors is enough to the MBSAS imaging proposed above, especially for the structure of point by point imaging algorithm that we can calculate each element's actual position. AUVs surveying in the deep water have a more stable working condition than the surface vessel. Although the application of GPS is limited underwater, USBL, DVL, INS, and compass are also optional sensors that can supply the motion parameters, which are widely equipped by AUVs such as HUGIN 1000. Compensation algorithms based on target echo or images, such as phase gradient autofocus (PGA) and displaced phase center (DPC) algorithms are also useful methods to manage the motion mismatch problem. They use the correlation of the echo overlapping phase center or focused iterative method to estimate the motion error of the carrier. Therefore, the moving trajectory of the carrier can be compensated that the practical application of MBSAS is possible.

MBSAS performs as a novel MBES with a higher along-track resolution that the application scenarios contain not only the traditional functions and purpose as water column, fish school, seabed surveying, but also the detailed imaging such as pipeline detecting, bottom target, and even the gas detecting. The flexible carriers including the surface vessel and the AUVs also expanded the application areas of MBSAS that it may become a new trend of imaging sonar. We have finished the modeling, target simulation, and imaging algorithm study as above and working for the motion estimation and field experiment in further research.

6. Conclusions

In this paper, we propose a novel underwater acoustic imaging scheme to improve the imaging performance of MBES, based on the complementarity of MBES and SAS systems. The MBSAS system is designed to enhance the performance of conventional underwater imaging instruments. The main research focuses on the complete theory of MBSAS, including the modeling, processing scheme, prototype design, target simulation, imaging algorithms, and experiment. The basic echo model of MBSAS and the processing scheme of the imaging system are analyzed and designed to meet engineering applications. A target with shadow area simulation approach is introduced according to the designed 2D array manifold. We also propose an imaging algorithm integrating the theories of MBES and SAS that provides high 3D full-scan resolution. The simulation results indicate that MBSAS can achieve higher resolution on the along-track than MBES. In addition, MBSAS overcomes the disadvantages of SAS and obtains 3D images with no gap problems. We can achieve more detailed

acoustic images by this approach than via the MBES system. A principle prototype of MBSAS is designed and produced to verify the novel theory proposed.

The feasibility and performance of the MBSAS modeling method and proposed imaging algorithm are demonstrated through a tank experiment. The experimental results indicate that MBSAS imaging can obtain constant resolution on the along-track. The MBSAS imaging method effectively separates adjusted targets with higher energy focusing ability, which is a great benefit to high-resolution sonar imaging systems. The MBSAS system will become a new trend in imaging sonar that can be widely employed in the field of underwater observation and detection. High resolution imaging algorithms and fast imaging schemes should be researched further to obtain more detailed 3D underwater acoustic images. Increasing the surveying efficiency through transducer array design and processing algorithms is a precondition of the wide extension of MBSAS. Designing and producing a practical detection instrument with powerful real-time processing ability is also an important foundation for engineering applications and large scene detection of MBSAS, based on the theoretical research above.

Author Contributions: Conceptualization, B.W. and T.Z.; Methodology, B.W. and H.L.; Software, B.W. and S.X.; Investigation, B.W. and T.Z.; Resources, H.L.; Writing—original draft preparation, B.W.; Writing—review and editing, B.W., H.L., T.Z., and S.X.; Visualization, B.Z. and S.X.; Supervision, T.Z. and H.L.; Project administration, T.Z.; Funding acquisition, H.L.

Funding: This work was funded by the National Natural Science Foundation of China under grant No. U1709203, 41606115, and 41376103; the National Key Research and Development Program of China under grant No. 2017YFC0306000; and the China State Shipbuilding Corporation Joint Foundation for Equipment Pre-Research under grant No. 6141B04060802.

Acknowledgments: The authors would like to thank the anonymous reviewers and editors for their constructive comments and suggestions.

Conflicts of Interest: The authors declare no conflict of interest.

References

1. Stateczny, A.; Wlodarczyk-Sielicka, M.; Gronska, D.; Motyl, W. Multibeam Echosounder and LiDAR in Process of 360-Degree Numerical Map Production for Restricted Waters with HydroDron. In Proceedings of the 2018 Baltic Geodetic Congress (BGC Geomatics), Olsztyn, Poland, 21–23 June 2018; pp. 288–292.
2. Gerlotto, F.; Soria, M.; Fréon, P. From two dimensions to three: The use of multibeam sonar for a new approach in fisheries acoustics. *Can. J. Fish. Aquat. Sci.* **1999**, *56*, 6–12. [CrossRef]
3. Clarke, J.E.H. Multibeam Water Column Imaging: Improved Wreck Least-Depth Determination. In Proceedings of the Canadian Hydrographic Conference, Halifax, NS, Canada, 5–9 June 2006.
4. Schneider von Deimling, J.; Weinrebe, W. Beyond Bathymetry: Water Column Imaging with Multibeam Echo Sounder Systems. *Hydrogr. Nachrichten* **2014**, *31*, 6–10.
5. Bellettini, A.; Pinto, M.A. Theoretical accuracy of synthetic aperture sonar micronavigation using a displaced phase-center antenna. *IEEE J. Ocean. Eng.* **2002**, *27*, 780–789. [CrossRef]
6. Bellettini, A.; Pinto, M.A. Design and Experimental Results of a 300-kHz Synthetic Aperture Sonar Optimized for Shallow-Water Operations. *IEEE J. Ocean. Eng.* **2009**, *34*, 285–293. [CrossRef]
7. Hagen, P.E. Gap filler sensors for SAS. In Proceedings of the OCEANS'11 MTS/IEEE KONA, Waikoloa, HI, USA, 19–22 September 2011; pp. 1–6.
8. Callow, H.J.; Hagen, P.E.; Hansen, R.E.; Sæbø, T.O.; Pedersen, R.B. A new approach to high-resolution seafloor mapping. *J. Ocean Technol.* **2012**, *7*, 13–22.
9. Bikonis, K.; Stepnowski, A.; Moszynski, M. Computer vision techniques applied for reconstruction of seafloor 3D images from side scan and synthetic aperture sonars data. In Proceedings of the 7th European Conference on Noise Control, Paris, France, 29 June–4 July 2008; pp. 4249–4254.
10. Qi, S. SAS azimuth precise by multi-iterative extrapolation. *J. Inf. Comput. Sci.* **2015**, *12*, 1417–1427. [CrossRef]
11. Zhang, X.; Tan, C.; Ying, W. An imaging algorithm for multireceiver synthetic aperture sonar. *Remote Sens.* **2019**, *11*, 672. [CrossRef]
12. Asada, A.; Yabuki, T. Synthetic aperture technique applied to a multi-beam echo sounder. *Earth Planets Space* **2001**, *53*, 321–326. [CrossRef]

13. Li, H.; Wei, B.; Du, W. Technical Progress in Research of Multibeam Synthetic Aperture Sonar. *Cehui Xuebao/Acta Geod. Cartogr. Sin.* **2017**, *46*, 1760–1769.
14. Wei, B.; Li, H.; Zhou, T.; Xu, C. Joint Motion Error Estimation Algorithm for Multibeam Synthetic Aperture Sonar. *IEEE Access* **2018**, *6*, 40519–40529. [CrossRef]
15. Pan, X.; Chen, Q.; Xu, W.; Li, J.; Sun, F. Shallow-water wideband low-frequency synthetic aperture sonar for an autonomous underwater vehicle. *Ocean Eng.* **2016**, *118*, 117–129. [CrossRef]
16. Kirkwood, K.P.; Korman, M.S. Computer simulation of synthetic aperture sonar for classroom demonstration. *Proc. Meet. Acoust.* **2017**, *30*, 045007.
17. Bird, J.S.; Mullins, G.K. Bathymetric sidescan sonar bottom estimation accuracy: Tilt angles and waveforms. *IEEE J. Ocean. Eng.* **2008**, *33*, 302–320. [CrossRef]
18. Jean, F. Several imaging algorithms for synthetic aperture sonar and forward looking gap-filler in real-time and post-processing on IXSEA's "Shadows" sonar. *J. Acoust. Soc. Am.* **2008**, *123*, 3906. [CrossRef]
19. Lopera, O.; Dupont, Y. Automated target recognition with SAS: Shadow and highlight-based classification. In Proceedings of the Oceans 2012, Hampton Roads, VA, USA, 14–19 October 2012.
20. Caporale, S.; Petillot, Y. A Novel Motion Compensation Approach for SAS. In Proceedings of the 2016 Sensor Signal Processing for Defence (SSPD), Edinburgh, UK, 22–23 September 2016; pp. 61–65.
21. Hunter, A.J.; Dugelay, S.; Fox, W.L.J. Repeat-Pass Synthetic Aperture Sonar Micronavigation Using Redundant Phase Center Arrays. *IEEE J. Ocean. Eng.* **2016**, *41*, 820–830. [CrossRef]
22. Wei, B.; Zhou, T.; Li, H.; Xing, T.; Li, Y. Theoretical and experimental study on multibeam synthetic aperture sonar. *J. Acoust. Soc. Am.* **2019**, *145*, 3177–3189. [CrossRef] [PubMed]
23. Pereira, D.J.; Hughes Clarke, J.E. Improving shallow water multibeam target detection at low grazing angles. In Proceedings of the US Hydrographic Conference, National Harbor, MD, USA, 16–19 March 2015; pp. 1–21.
24. De Moustier, C. Time and angle of arrival uncertainties in echo sounding. In Proceedings of the Oceans 2011, Santander, Spain, 6–9 June 2011; pp. 1–4.
25. Yang, Y.; Jiao, J. Phase Difference Technology Apply to the Sounding of Broadband Multi-Beam Bathymetry Sonar. In Proceedings of the 2016 IEEE/OES China Ocean Acoustics Symposium (COA), Harbin, China, 9–11 January 2016; pp. 1–6.
26. Yang, T.C. Deconvolved Conventional Beamforming for a Horizontal Line Array. *IEEE J. Ocean. Eng.* **2018**, *43*, 160–172. [CrossRef]
27. Levanda, R.; Leshem, A. Adaptive selective sidelobe canceller beamformer with applications to interference mitigation in radio astronomy. *IEEE Trans. Signal Process.* **2013**, *61*, 5063–5074. [CrossRef]